

First-principles calculations for ferroelectrics at constant polarization using generalized Wannier functions

Paweł Lenarczyk* and Mathieu Luisier

Integrated Systems Laboratory, ETH Zürich, 8092 Zürich, Switzerland

(Dated: March 13, 2024)

Localized Wannier functions provide an efficient and intuitive framework to compute electric polarization from first-principles. They can also be used to represent the electronic systems at fixed electric field and to determine dielectric properties of insulating materials. Here we develop a Wannier-function-based formalism to perform first-principles calculations at fixed polarization. Such an approach allows to extract the polarization-energy landscape of a crystal and thus supports the theoretical investigation of polar materials. To facilitate the calculations, we implement a quasi-Newton method that simultaneously relaxes the internal coordinates and adjusts the electric field in crystals at fixed polarization. The method is applied to study the ferroelectric behavior of BaTiO₃ and PbTiO₃ in tetragonal phases. The physical processes driving the ferroelectricity of both compounds are examined thanks to the localized orbital picture offered by Wannier functions. Hence, changes in chemical bonding under ferroelectric distortion can be accurately visualized. The difference in the ferroelectric properties of BaTiO₃ and PbTiO₃ is highlighted. It can be traced back to the peculiarities of their electronic structures.

PACS numbers: 71.15.-m, 71.15.Ap, 77.80.-e, 77.22.Ej

I. INTRODUCTION

The development of the microscopic modern theory of polarization^{1–3} (MTP) has enabled significant progresses in the understanding of ferroelectric states. MTP rigorously defines the polarization of a periodic solid and provides a route for its computation using electronic structure methods such as density functional theory⁴ (DFT). Thus, many properties that could previously be inferred only at a very qualitative level can now be computed with quantum mechanical accuracy from first-principles.

MTP is also a basis for the development of techniques to determine the exact ground state of a crystalline insulator in the presence of an electric field \mathcal{E} . This is realized^{5–7} by minimizing the electric enthalpy functional composed of the usual Kohn-Sham energy and a field coupling term: “ $\mathcal{E} \cdot \mathbf{P}$ ”, involving the electric polarization \mathbf{P} . In particular, it has been shown by the authors in Ref. 8 that non-orthogonal generalized Wannier functions provide efficient and intuitive means by which to perform finite-field calculations within a DFT framework. It is therefore possible to calculate from first-principles many interesting properties of materials related to their behavior under external electric fields.

In this paper we present a method for performing first-principles calculations not at constant electric field, but at fixed electric polarization. This enables to compute crystal properties as a function of \mathbf{P} , providing a way to extract the polarization-energy landscape $E(\mathbf{P})$ of any material. Knowing $E(\mathbf{P})$, its dielectric or ferroelectric properties can be inferred. Moreover, constrained- \mathbf{P} calculations make it simultaneously possible to exhibit and understand the dynamical transformations of the system under study, which can lead to a particular electrical behavior. In addition to first-principles investigations, the ability to compute $E(\mathbf{P})$ within DFT provides an

intuitive link to Landau-Devonshire (LD) semiempirical theory⁹ in which \mathbf{P} serves as an order parameter. Hence, the constrained- \mathbf{P} method may pave the way for the first-principles derivation of LD descriptions for a wide range of ferroelectric materials. This could be useful, for example, in the context of ferroelectric device simulations.¹⁰

Our approach partly derives inspiration from the work of Sai, Rabe, and Vanderbilt (SRV) on the structural response to macroscopic electric fields in ferroelectric systems.¹¹ By using density functional perturbation theory (DFPT) these authors constructed an approximate thermodynamic potential whose minimization with respect to internal structural parameters produces crystal structures at fixed polarization. In the SRV approach both the internal energy and the electric polarization are evaluated at zero electric field. The effect of the electric field on the electronic structure is therefore neglected. This limitation of the SRV method was addressed by Dieguez and Vanderbilt¹² (DV) who overcome it by employing the theory of finite electric fields developed by Souza, Iniguez, and Vanderbilt⁶ (SIV). The DV method is thus an exact one. However, because it incorporates the reciprocal-space-based SIV theory of finite electric fields, Brillouin zone sampling may be restricted to eliminate the possibility of runaway solutions,^{6,13} i.e., to allow for stable stationary solutions to exist. This is especially problematic when it comes to the calculation of ferroelectric properties, which are known to be sensitive to the quality of the Brillouin zone integration and require large k -point sets to converge.^{14,15}

Instead, we base our constrained- \mathbf{P} method on the first-principles theory of finite electric fields proposed by Nunes and Vanderbilt⁵ (NV). These authors showed in Ref. 5 that a real-space representation of occupied subspace in terms of orthogonal Wannier-functions (WFs) could be used to calculate the internal energy and the

electric polarization of a periodic insulator in the presence of a finite electric field. In particular, we rely on our extension of this theory to employ non-orthogonal generalized Wannier functions (NGWFs), as implemented in Ref. 8. The purpose is twofold: apart from its computational efficiency, such a formulation readily allows for an intuitive understanding of the effects of the polarization. As will become clear below, this is possible by employing a Wannier-like representation of the electronic structure. Moreover, this description provides an insightful picture of the nature of the chemical bonds in materials,¹⁶ otherwise missing from the picture of extended eigenstates: insightful chemical analyses of the nature of bonding can be performed, as well as its evolution during ferroelectric transitions. Finally, the mechanism of polarization as electronic currents produced by dynamical changes of orbital hybridizations can be visualized, helping to clarify the origin of ferroelectricity in polar materials.

The plan of the remainder of this paper is as follows. In the next section, the details of the general theoretical framework are presented. The practical implementation of the method is then discussed in Sec. III. In Sec. IV a description of the quasi-Newton algorithm for constrained polarization calculations is given. The systems analyzed in this work are described in Sec. V, including a discussion of the technical details of the *ab initio* pseudopotential calculations. Then, in Sec. VI, we report the results of our calculations, starting in Sec. VIA with the tests that have been performed to probe the practical usefulness of the method. The method is then applied in Sec. VIB and VIC to study the ferroelectricity of tetragonal BaTiO₃ and PbTiO₃, respectively. The $E(\mathbf{P})$ characteristics are obtained and associated with dynamical transformations of the crystal and electronic structures at fixed polarization. Localized Wannier functions are used to investigate the changes in chemical bonding that lead to the stabilization of a ferroelectric distortion for both compounds. We also highlight the differences in the ferroelectric behavior of BaTiO₃ and PbTiO₃ that come from their different electronic structures. Finally, in Sec. VII, we summarize and conclude our work.

Atomic (Rydberg) units are used throughout this paper, unless explicitly stated, i.e., $\bar{e} = \hbar = m_e = 1$, length unit $r_B = 0.53\text{\AA}$, energy unit $Ry = 13.6\text{eV}$.

II. FORMALISM

We will now describe a formalism to perform first-principles calculations at constant polarization. Our approach replicates some of the ideas of the SIV perturbative scheme,¹¹ but results instead in an exact method since it incorporates the NV theory of finite electric fields.⁵ Moreover, in the derivation presented below forces due to polarization constraint appear in a more natural way than in the SIV approach.

Let ρ be the electron density and $\boldsymbol{\tau}$ the atomic coordinates. Consider a periodic insulating crystal with a

unit cell volume Ω . In the context of electronic structure calculations, the electric enthalpy is given by^{5-8,13}

$$W[\rho](\boldsymbol{\tau}, \boldsymbol{\mathcal{E}}) = E_{KS}[\rho](\boldsymbol{\tau}) - \Omega \boldsymbol{\mathcal{E}} \cdot \mathbf{P}[\rho](\boldsymbol{\tau}) . \quad (1)$$

Here $E_{KS}[\rho](\boldsymbol{\tau})$ stands for the usual Kohn-Sham (KS) energy per unit cell. The above equation must be minimized with respect to the density functions ρ in order to find the electronic ground state in the presence of an electric field

$$\begin{aligned} W_{gs}(\boldsymbol{\tau}, \boldsymbol{\mathcal{E}}) &= \min_{\rho} W[\rho](\boldsymbol{\tau}, \boldsymbol{\mathcal{E}}) \\ &= E_{KS}(\boldsymbol{\tau}) - \Omega \boldsymbol{\mathcal{E}} \cdot \mathbf{P}(\boldsymbol{\tau}) . \end{aligned} \quad (2)$$

This solution corresponds to a polarized long-lived resonant state of a periodic insulating solid, where the intraband (or Zener) tunneling is neglected.^{5,6,13} The functional $W_{gs}(\boldsymbol{\tau}, \boldsymbol{\mathcal{E}})$ can be viewed as a thermodynamic potential that minimizes to equilibrium values the coordinates $\boldsymbol{\tau}$ at fixed $\boldsymbol{\mathcal{E}}$.

An approach to solve this finite-field problem, given by the minimization of the electric enthalpy Eq. (2) with respect to the field-dependent density functions, was proposed by NV in Ref. 5. In the NV theory of finite-electric fields a representation of the density functions in terms of truncated field-polarized Wannier functions is employed to write a functional for the band-structure energy and the electronic polarization of a solid in a uniform electric field. This scheme has been implemented in a DFT framework in Ref. 8, where an overview of the method is given in Sec. 2, for *ab initio* force calculations in the presence of electric fields.

Our goal in this work is to perform calculations at a given polarization target value \mathbf{P}_t . This can be achieved via a Legendre transformation of the electric enthalpy $W_{gs}(\boldsymbol{\tau}, \boldsymbol{\mathcal{E}})$ to a thermodynamic potential $E_{gs}(\boldsymbol{\tau}, \mathbf{P}_t)$ in which the polarization is the control parameter and the electric field the state variable

$$E_{gs}(\boldsymbol{\tau}, \mathbf{P}_t) = \min_{\boldsymbol{\mathcal{E}}} \{W_{gs}(\boldsymbol{\tau}, \boldsymbol{\mathcal{E}}) + \Omega \boldsymbol{\mathcal{E}} \cdot \mathbf{P}_t\} . \quad (3)$$

The thermodynamic potential $E_{gs}(\boldsymbol{\tau}, \mathbf{P}_t)$ can be minimized with respect to the atomic coordinates $\boldsymbol{\tau}$, which leads to the energy $E(\mathbf{P}_t)$, a functional of polarization

$$\begin{aligned} E(\mathbf{P}_t) &= \min_{\boldsymbol{\tau}} E_{gs}(\boldsymbol{\tau}, \mathbf{P}_t) \\ &= \min_{\boldsymbol{\tau}, \boldsymbol{\mathcal{E}}} \{E_{KS}(\boldsymbol{\tau}) - \Omega \boldsymbol{\mathcal{E}} \cdot (\mathbf{P}(\boldsymbol{\tau}) - \mathbf{P}_t)\} . \end{aligned} \quad (4)$$

This minimization allows to determine the structural properties of the system under study at a fixed polarization \mathbf{P}_t . As it can be seen, the expression in Eq. (4) can also be interpreted as one where $\boldsymbol{\mathcal{E}}$ represents a Lagrange multiplier implementing the constraint $\mathbf{P}(\boldsymbol{\tau}) = \mathbf{P}_t$.

The governing equations of the constrained polarization calculations can be derived by applying the variational principle.¹⁷ Consider a change of the objective function in Eq. (4), induced by a variation of the $\boldsymbol{\tau}$ and

\mathcal{E} variables, what is equal to zero at the minimum

$$\left. \frac{dE_{\text{gs}}(\boldsymbol{\tau}, \boldsymbol{\mathcal{E}})}{d\boldsymbol{\tau}} \right|_{\boldsymbol{\mathcal{E}}} \cdot \delta\boldsymbol{\tau} - \Omega(\mathbf{P}(\boldsymbol{\tau}) - \mathbf{P}_t) \cdot \delta\boldsymbol{\mathcal{E}} = 0. \quad (5)$$

By using the fact that the system is brought to the Born-Oppenheimer surface after the electronic minimization in Eq. (2), the Hellmann-Feynman theorem^{18,19} can be invoked. This allows to take into account only the explicit dependence of the electric enthalpy on the atomic coordinates when calculating the corresponding derivatives

$$\left. \frac{dW_{\text{gs}}(\boldsymbol{\tau}, \boldsymbol{\mathcal{E}})}{d\boldsymbol{\tau}} \right|_{\boldsymbol{\mathcal{E}}} = \frac{\partial E_{\text{KS}}(\boldsymbol{\tau})}{\partial \boldsymbol{\tau}} - \Omega \boldsymbol{\mathcal{E}} \frac{\partial \mathbf{P}(\boldsymbol{\tau})}{\partial \boldsymbol{\tau}}. \quad (6)$$

In the above equation, the first term on the right-hand side is just the negative of the force, as calculated in ordinary KS theory

$$\mathbf{F}_{\text{KS}}(\boldsymbol{\tau}) = - \frac{\partial E_{\text{KS}}(\boldsymbol{\tau})}{\partial \boldsymbol{\tau}}. \quad (7)$$

The second term is the force due to the polarization constraint

$$\mathbf{F}_{\mathcal{E}}(\boldsymbol{\tau}, \boldsymbol{\mathcal{E}}) = \Omega \boldsymbol{\mathcal{E}} \frac{\partial \mathbf{P}(\boldsymbol{\tau})}{\partial \boldsymbol{\tau}}. \quad (8)$$

Therefore, it can be seen that by using the variational principle the total force

$$\mathbf{F}(\boldsymbol{\tau}, \boldsymbol{\mathcal{E}}) = \mathbf{F}_{\text{KS}}(\boldsymbol{\tau}) + \mathbf{F}_{\mathcal{E}}(\boldsymbol{\tau}, \boldsymbol{\mathcal{E}}), \quad (9)$$

which is composed of a KS and electric field contribution, naturally emerges in our formulation. Practical implementation of both force terms within Wannier-function theory of finite-electric fields will be discussed in Sec. III.

Since Eq. (5) must hold for arbitrary $\delta\boldsymbol{\tau}$ and $\delta\boldsymbol{\mathcal{E}}$ it gives after substituting Eqs. (6)–(9) the following system of equations

$$\begin{cases} \mathbf{F}(\boldsymbol{\tau}, \boldsymbol{\mathcal{E}}) = \mathbf{0} \\ \mathbf{P}(\boldsymbol{\tau}) - \mathbf{P}_t = \mathbf{0} \end{cases}, \quad (10)$$

which can be solved for $\boldsymbol{\tau}$ and $\boldsymbol{\mathcal{E}}$. Note that Eq. (10) corresponds to the Euler-Lagrange equation¹⁷ of the $E(\mathbf{P}_t)$ functional. The developed algorithm to solve Eq. (10) and subsequently find the stationary point of $E(\mathbf{P}_t)$ will be presented in Sec. IV.

As it can be seen from the coupled system of equations (10), the first equation requires that the total forces acting on the atoms vanish and the second equation ensures that the polarization constraint is fulfilled, at the end of the geometry optimization. As it can be deduced from Eq. (4), after solving Eq. (10), we find

$$E(\mathbf{P}_t) = E_{\text{KS}}(\boldsymbol{\tau}(\mathbf{P}_t)). \quad (11)$$

Consequently, by solving Eq. (10) the potential energy landscape of a solid can be examined as a function of its polarization.

III. CALCULATION OF TOTAL ENERGY, POLARIZATION, AND FORCES

It is not entirely straightforward to compute the ground state of a bulk solid in the presence of an electric field, as required by Eq. (2). The difficulty of treating finite electric fields is related to the definition of a polarization for a periodic system.²⁰ The development of the modern theory of polarization^{1–3} has been at the origin of significant recent progresses with that respect and has enabled the application of electric fields in periodic electronic structure calculations.^{5–7} In particular, NV have shown that localized WFs can be used to describe a periodic insulating solid in the presence of a uniform electric field.⁵

The NV theory of finite electric fields and electronic polarization can be extended to the case of non-orthogonal generalized WFs (NGWFs) to improve convergence in practical calculations.⁸ The latter approach relies on the following parametrization of the density operator

$$\hat{\rho} = \sum_{\substack{ij \\ ab}} |\nu_a^i\rangle K_{ab}^{ij} \langle \nu_b^j|, \quad (12)$$

written in terms of the localized, Wannier-like orbitals $\{\nu_a^i\}$ and the elements of the density kernel matrix $\{K_{ab}^{ij}\}$, where the superscript indices i, j denote the cell replicas, and subscript indices a, b the occupied bands. The periodicity of the electronic state is expressed as $|\nu_a^i\rangle = \hat{T}_{\mathbf{R}_i} |\nu_a^0\rangle$, where $\hat{T}_{\mathbf{R}_i}$ is the translation operator corresponding to the lattice vector \mathbf{R}_i and the superscript 0 indicates that the orbital is centered in the unit cell containing the origin. For the density kernel matrix it holds $K_{ab}^{ij} = K_{ab}(\mathbf{R}_j - \mathbf{R}_i)$.¹⁶

By taking Eq. (12) as an ansatz for a trial density operator, the physical density operator $\hat{\rho}'$ is derived by employing the McWeeny purifying transformation.²¹ This ensures a weak idempotency of $\hat{\rho}'$ so that it can be used to describe the occupied space. In this approach the expectation value of any operator \hat{O} is given by $\text{tr}[\hat{\rho}'\hat{O}]$. The trace over the occupied space can be conveniently evaluated by introducing the auxiliary wave functions

$$|\tilde{\nu}_b^j\rangle = \sum_i Q_{ba}^{ji} |\nu_a^i\rangle, \quad (13)$$

where $Q_{ab}^{ij} = 2K_{ab}^{ij} - (\mathbf{K} \times \mathbf{S} \times \mathbf{K})_{ab}^{ij}$ and $S_{ab}^{ij} = \langle \nu_a^i | \nu_b^j \rangle$, the overlap matrix between the orbitals. For the derivation of the \mathbf{Q} matrix, see Ref. 8. The $\{|\tilde{\nu}_b^j\rangle\}$ set constitutes the biorthogonal complement²² to $\{|\nu_a^i\rangle\}$, which satisfies the biorthogonality relationship $\langle \nu_a^i | \tilde{\nu}_b^j \rangle = \delta_{ij} \delta_{ab}$.

In this formulation the band structure energy E_{bs} , which corresponds to the expectation value of the Hamiltonian operator \hat{H} , is evaluated as

$$E_{bs}[\hat{\rho}'](\boldsymbol{\tau}) = 2 \sum_a \langle \nu_a | \hat{H}(\boldsymbol{\tau}) | \tilde{\nu}_a \rangle. \quad (14)$$

The electronic contribution \mathbf{P}_{el} to the macroscopic polarization \mathbf{P} is related to the expectation value of the position operator,²³ $\hat{\mathbf{r}}$. In the present formalism it can be simply calculated as the sum of the centroids of charge of the localized orbitals, scaled by the volume of the unit cell Ω

$$\mathbf{P}_{el}[\hat{\rho}'] = -\frac{2}{\Omega} \sum_a \langle \nu_a | \hat{\mathbf{r}} | \tilde{\nu}_a \rangle . \quad (15)$$

Note that the above equation is equivalent to the expression for the electronic contribution to the polarization in the Berry-phase theory, through the formal connections between the centers of charge of the WFs and the Berry phases of the Bloch functions as they are carried around the Brillouin zone.²³

The electron density is the diagonal of the physical density matrix. In the present formalism it can be evaluated as

$$\rho(\mathbf{r}) = 2 \sum_a \langle \nu_a | \mathbf{r} \rangle \langle \mathbf{r} | \tilde{\nu}_a \rangle , \quad (16)$$

where the factor 2 takes into account the assumed spin degeneracy. In Eqs. (14)–(16) and in the following, the superscript indicating the cell replica has been dropped so that $\nu_a \equiv \nu_a^0$.

The Kohn-Sham total energy E_{KS} can now be written in terms of the degrees of freedom of the density, as a sum of the band-structure energy E_{bs} in Eq. (14), minus the double-count correction term E_{dc} and plus the classical electrostatic energy among the ions E_{i-i} , i.e.

$$E_{KS}[\hat{\rho}'](\boldsymbol{\tau}) = E_{bs}[\hat{\rho}'](\boldsymbol{\tau}) - E_{dc}[\hat{\rho}'] + E_{i-i}(\boldsymbol{\tau}) . \quad (17)$$

To obtain the total polarization, the classical ionic contribution \mathbf{P}_{ion} must be added to Eq. (15). The total polarization \mathbf{P} is then

$$\mathbf{P}[\hat{\rho}'](\boldsymbol{\tau}) = \mathbf{P}_{el}[\hat{\rho}'] + \mathbf{P}_{ion}(\boldsymbol{\tau}) . \quad (18)$$

In the pseudopotential approximation employed in this work the \mathbf{P}_{ion} term arises from the sum of the ionic core point charges Q_I located at the corresponding atomic positions $\boldsymbol{\tau}_I$

$$\mathbf{P}_{ion}(\boldsymbol{\tau}) = \frac{1}{\Omega} \sum_I Q_I \boldsymbol{\tau}_I . \quad (19)$$

By substituting Eqs. (17) and (18) into Eq. (1) the minimization with respect to the degrees of freedom of the physical density matrix, $\{\nu_a^0\}$ and $\{K_{ab}^{0i}\}$, can be carried out to determine the ground state of a solid in the presence of a fixed electric field. In our implementation of the above outlined formalism the localized orbitals are represented on a uniform real-space grid and $\langle \mathbf{r} | \nu_a^0 \rangle$ is allowed to be nonzero only inside cubic regions with size a_{LR} , referred to as the localization regions (LRs) in the following.

At the end of the electronic minimization, the Hellmann-Feynman forces in Eqs. (7), (8) can be evaluated by invoking the expressions for the total energy in Eq. (17) and polarization in Eq. (18), as discussed above. It should be noted that because the localized orbitals are optimized *in situ* on fixed grids, there is no force contribution due to the explicit dependence of the basis set on the atomic position — known as Pulay forces.²⁴

According to Eq. (17) the KS forces can be separated into two parts, \mathbf{F}_{bs} coming from the band-structure energy term, E_{bs} , and \mathbf{F}_{i-i} associated with the ion-ion energy term, E_{i-i} . Thus, the KS force of the intra- and interatomic interaction acting on the I th atom, located at $\boldsymbol{\tau}_I$, can be written as

$$\mathbf{F}_{KS}(\boldsymbol{\tau}_I) = \mathbf{F}_{bs}(\boldsymbol{\tau}_I) + \mathbf{F}_{i-i}(\boldsymbol{\tau}_I) . \quad (20)$$

The force $\mathbf{F}_{i-i}(\boldsymbol{\tau}_I)$ exerted on one ion by all the other ions can be evaluated as usual in periodic systems by performing two convergent summations, one over the lattice vectors and the other one over the reciprocal-lattice vectors, using Ewald's method.²⁵

If the basis set used to represent the electronic degrees of freedom is independent of the atomic coordinates, as in our case, \mathbf{F}_{bs} is solely due to the explicit dependence of the Hamiltonian on the position of the atoms. Among the components of the KS Hamiltonian, only the ionic potential, V_{ion} , is a function of $\boldsymbol{\tau}$, thus $\mathbf{F}_{bs} = \mathbf{F}_{ion}$. This term is evaluated using the pseudopotential theory. We employ nonlocal norm-conserving ionic pseudopotentials cast in the Kleinman-Bylander form.²⁶ The ionic pseudopotential due to an atom I at position $\boldsymbol{\tau}_I$, $\hat{V}_{ion}(\boldsymbol{\tau}_I)$, is obtained as the sum of a local, $\hat{V}_{loc}(\boldsymbol{\tau}_I)$, and nonlocal, $\hat{V}_{nloc}(\boldsymbol{\tau}_I)$ term, the latter corresponding to an angular-momentum-dependent projection.²⁶ Like the pseudopotential energy itself, the pseudopotential force is the sum of local and nonlocal parts: $\mathbf{F}_{ion} = \mathbf{F}_{loc} + \mathbf{F}_{nloc}$. The local pseudopotential force is given by

$$\mathbf{F}_{loc}(\boldsymbol{\tau}_I) = -2 \frac{\partial}{\partial \boldsymbol{\tau}_I} \sum_a \langle \nu_a | \hat{V}_{loc}(\boldsymbol{\tau}_I) | \tilde{\nu}_a \rangle . \quad (21)$$

The force component $\mathbf{F}_{loc}(\boldsymbol{\tau}_I)$ can be calculated as usual by evaluating the expectation value of the derivative of the ionic potential with respect to the ionic position.²⁷ Because $\frac{\partial \hat{V}_{loc}(\boldsymbol{\tau}_I)}{\partial \boldsymbol{\tau}_I}$ is local, this reduces to the integration of this term, multiplied by the electron density, over a grid spanning the simulation cell.

It is however advantageous to consider a different implementation of \mathbf{F}_{loc} .^{28,29} Starting from Eq. (21), by changing the integration variable $\mathbf{r} \rightarrow \mathbf{r}' = \mathbf{r} - \boldsymbol{\tau}_I$, when evaluating the matrix elements $\langle \nu_a | \hat{V}_{loc}(\boldsymbol{\tau}_I) | \tilde{\nu}_a \rangle$, the a th orbital contribution to the local pseudopotential force on the I th ion can be written as

$$\begin{aligned} \frac{\partial}{\partial \boldsymbol{\tau}_I} \langle \nu_a | \hat{V}_{loc}(\boldsymbol{\tau}_I) | \tilde{\nu}_a \rangle = \\ \int_{LR_a} \frac{\partial}{\partial \boldsymbol{\tau}_I} \nu_a(\mathbf{r}' + \boldsymbol{\tau}_I) V_{loc}(\mathbf{r}') \tilde{\nu}_a(\mathbf{r}' + \boldsymbol{\tau}_I) d\mathbf{r}' . \end{aligned} \quad (22)$$

It follows from Eq. (22) that with the transformation of the variable \mathbf{r}' back to $\mathbf{r} = \mathbf{r}' + \boldsymbol{\tau}_I$, the local pseudopotential force can be calculated as

$$\mathbf{F}_{\text{loc}}(\boldsymbol{\tau}_I) = -2 \sum_a \left[\langle \nabla_{\mathbf{r}} \nu_a | \hat{V}_{\text{loc}}(\boldsymbol{\tau}_I) | \tilde{\nu}_a \rangle + \langle \nu_a | \hat{V}_{\text{loc}}(\boldsymbol{\tau}_I) | \nabla_{\mathbf{r}} \tilde{\nu}_a \rangle \right]. \quad (23)$$

This is the formula for the local pseudopotential force employed in our implementation.

Along the same line as in Eq. (23), an analogous expression can be derived for the nonlocal pseudopotential force. The contribution to the force on atom I coming from the nonlocal components of the pseudopotential is

$$\mathbf{F}_{\text{nloc}}(\boldsymbol{\tau}_I) = -2 \frac{\partial}{\partial \boldsymbol{\tau}_I} \sum_a \sum_{l,m} \langle \nu_a | \phi_{lm}(\boldsymbol{\tau}_I) \rangle \langle \phi_{lm}(\boldsymbol{\tau}_I) | \tilde{\nu}_a \rangle, \quad (24)$$

where $\phi_{lm}(\boldsymbol{\tau}_I)$ are the projector functions on atom I , running over angular momentum indices l, m .

By applying the $\mathbf{r} \rightarrow \mathbf{r}' = \mathbf{r} - \boldsymbol{\tau}_I$ transformation when evaluating the projection coefficients $\langle \phi_{lm}(\boldsymbol{\tau}_I) | \nu_a \rangle$ and integrating over the core regions of the I th base atom replicas entering the a th orbital localization region, the following formula for the nonlocal pseudopotential force is obtained

$$\mathbf{F}_{\text{loc}}(\boldsymbol{\tau}_I) = -2 \sum_a \sum_{l,m} \left[\langle \nabla_{\mathbf{r}} \nu_a | \phi_{lm}(\boldsymbol{\tau}_I) \rangle \langle \phi_{lm}(\boldsymbol{\tau}_I) | \tilde{\nu}_a \rangle + \langle \nu_a | \phi_{lm}(\boldsymbol{\tau}_I) \rangle \langle \phi_{lm}(\boldsymbol{\tau}_I) | \nabla_{\mathbf{r}} \tilde{\nu}_a \rangle \right]. \quad (25)$$

Our motivation for using this alternative ionic force formulation, which does not include the derivative of the ionic potential, but the gradient of the real-space wave functions, as in Eqs. (23) and (25), is that it is more precise when discretized on a grid. This finding was reported in Ref. 29, in the context of molecular calculations employing local ionic potentials. The reason for the improved accuracy can be attributed to the wave functions that are generally smoother than the ionic potential, so that their derivatives can be better represented on a grid. The erroneous effect coming from the real-space discretization can be further reduced by employing the pseudopotential filtering technique.³⁰ It eliminates the Fourier components of the local potential and the projector functions that cannot be represented on the grid. As an overall result, the convergence of the force calculations with respect to the grid spacing is improved. This is important in view of the observed moderate convergence of the pseudopotential forces with respect to the LR size of the orbitals, on which the grids are spanned, and will be further discussed in Sec. VI A.

We now turn to the calculation of the force term $\mathbf{F}_{\mathcal{E}}$ associated with the polarization constraint. Following the

Hellmann-Feynman argument $\mathbf{F}_{\mathcal{E}}$ can be evaluated according to Eq. (8), which involves only the partial derivatives $\frac{\partial \mathbf{P}}{\partial \boldsymbol{\tau}_I}$ of the polarization \mathbf{P} in Eq. (18) with respect to the atomic coordinates $\{\boldsymbol{\tau}_I\}$. Since we use a basis set independent of $\boldsymbol{\tau}_I$ and employ norm-conserving pseudopotentials in our calculations, the only explicit dependence of the polarization in Eq. (18) on $\boldsymbol{\tau}_I$ comes from the ionic term \mathbf{P}_{ion} given by Eq. (19). This is not true when using ultra-soft pseudopotentials, which need additional augmentation terms in the expression for the electronic polarization,³¹ with the explicit dependence on the atomic coordinates. However, in our case, $\frac{\partial \mathbf{P}}{\partial \boldsymbol{\tau}_I} = \frac{\partial \mathbf{P}_{\text{ion}}}{\partial \boldsymbol{\tau}_I}$, and consequently the force due to the polarization constraint, acting on atom I is given by

$$\mathbf{F}_{\mathcal{E}}(\boldsymbol{\tau}_I) = \mathcal{E} Q_I. \quad (26)$$

As is apparent from Eq. (26) the $\mathbf{F}_{\mathcal{E}}(\boldsymbol{\tau}_I)$ term is the force induced by the electric field \mathcal{E} acting on a point ionic core charge Q_I . The same expression is used in finite-field calculations,^{6,7} but here, $\mathbf{F}_{\mathcal{E}}$ shall be interpreted as a constraint force with the electric field \mathcal{E} playing the role of a Lagrange multiplier imposing the polarization constraint.

IV. SOLUTION ALGORITHM

In this section an optimization method is proposed that allows to simultaneously relax the atomic coordinates and adjust the electric field so that the stationary point of the energy functional of the polarization, $E(\mathbf{P}_t)$, can be found. The technique is based on the application of the quasi-Newton scheme of Vanderbilt and Louie³² (VL) to iteratively solve Eq. (10). The advantage of the proposed approach is that it does not require the second derivatives of the enthalpy, which cannot be calculated analytically within DFT. This is in contrast to the SRV method, which uses DFPT to obtain the guiding tensors in the minimization procedure over structural degrees of freedom that gives the target polarization.^{11,12}

With the VL scheme the roots of a vector function $\mathbf{f}(\mathbf{x})$ of a vector variable \mathbf{x} can be determined. In the case of Eq. (10), we define

$$\mathbf{x} := [\boldsymbol{\tau} \quad \mathcal{E}]^{\top} \quad (27)$$

and

$$\mathbf{f} := [\mathbf{F} \quad \Omega \Delta \mathbf{P}]^{\top}, \quad (28)$$

where $\Delta \mathbf{P} = \mathbf{P} - \mathbf{P}_t$.

The goal is now to find \mathbf{x} such that $\mathbf{f}(\mathbf{x}) = \mathbf{0}$. For a generally non-linear function $\mathbf{f}(\mathbf{x})$, as in our case, this is done iteratively. Starting from an initial guess $\mathbf{x}^{(0)}$ and $\mathbf{f}^{(0)} = \mathbf{f}(\mathbf{x}^{(0)})$, it can be predicted that on the m th iteration, in linear order, a new $\mathbf{x}^{(m+1)}$ will result in a $\mathbf{f}^{(m+1)}$ satisfying the following secant equation³³

$$\mathbf{f}^{(m+1)} - \mathbf{f}^{(m)} = -\mathbf{J} \times (\mathbf{x}^{(m+1)} - \mathbf{x}^{(m)}), \quad (29)$$

where the Jacobian is defined as

$$\mathbf{J} = -\frac{d\mathbf{f}}{d\mathbf{x}}. \quad (30)$$

By setting $\mathbf{f}^{(m+1)} = \mathbf{0}$, which is the goal of the optimization, gives the Newton step

$$\mathbf{x}^{(m+1)} = \mathbf{x}^{(m)} + [\mathbf{J}^{(m)}]^{-1} \times \mathbf{f}^{(m)}. \quad (31)$$

Eq. (31) can be used to carry out the optimization by iteratively improving the solution vector \mathbf{x} , if the Jacobian is known.

For the constrained polarization calculation case the Jacobian matrix in Eq. (30) is composed of the following blocks

$$\mathbf{J} = \begin{bmatrix} \mathbf{K} & -\mathbf{Z} \\ -\mathbf{Z} & -\Omega\chi \end{bmatrix}, \quad (32)$$

which correspond to the different components of the \mathbf{f} and \mathbf{x} vectors specified in Eqs. (28) and (27), respectively. These blocks have the following interpretation: $\mathbf{K} := -\frac{d\mathbf{F}}{d\boldsymbol{\tau}}$ is the force-constant matrix; $\chi := \frac{d\mathbf{P}}{d\boldsymbol{\mathcal{E}}}$ is the susceptibility tensor; $\mathbf{Z} := \frac{d\mathbf{F}}{d\boldsymbol{\mathcal{E}}}$ is the Born effective charge tensor. Note that the \mathbf{Z} matrix can be re-expressed as $\mathbf{Z} = -\frac{d^2 E_{gs}(\boldsymbol{\tau}, \boldsymbol{\mathcal{E}})}{d\boldsymbol{\tau} d\boldsymbol{\mathcal{E}}} = \Omega \frac{d\mathbf{P}}{d\boldsymbol{\tau}}$ (see Eqs. (2) and (6)), which is used to substitute the second row in Eq. (32).

The matrices \mathbf{K} , χ , and \mathbf{Z} needed to form the Jacobian in Eq. (32) cannot be calculated analytically within DFT because the forces and the polarization are not variational. Since these matrices are of interest by themselves, for studying the elastic and electric properties of materials, DFPT techniques were developed to approximate them. These methods consist however of rather involved expressions which must be carefully handled in the presence of electric fields.³⁴ They further require special implementations³⁵. An other common approach to calculate the elements of the force-constant matrix³⁶, dielectric, and Born effective charge tensors³⁷ is by numerical differentiation, but this is not computationally efficient for the present purposes.

We propose here to use the VL approach and build up the Jacobian through iterative improvements by employing the information from the previous iterations of the optimization algorithm. Specifically, the Jacobian $\mathbf{J}^{(m+1)}$ is constructed by requiring that it satisfies in the least-square sense the secant Eq. (29) for the m previous iterations. An additional weighted condition stating that $\mathbf{J}^{(m+1)}$ makes the least change to the initial Jacobian $\mathbf{J}^{(0)}$ is also imposed

$$S = \sum_{l=0}^m w^{(l)} \left| \mathbf{J}^{(m+1)} \times \Delta \mathbf{x}^{(l)} + \Delta \mathbf{f}^{(l)} \right|^2 + w^{(0)} \left\| \mathbf{J}^{(m+1)} - \mathbf{J}^{(0)} \right\|^2, \quad (33)$$

where $\Delta \mathbf{x}^{(l)} = (\mathbf{x}^{(l+1)} - \mathbf{x}^{(l)}) / |\mathbf{x}^{(l+1)} - \mathbf{x}^{(l)}|$ and $\Delta \mathbf{f}^{(l)} = (\mathbf{f}^{(l+1)} - \mathbf{f}^{(l)}) / |\mathbf{f}^{(l+1)} - \mathbf{f}^{(l)}|$ represent the

normalized differences of the successive iterations. We use $|\mathbf{x}|$ to denote the L^2 -norm of a vector \mathbf{x} ($|\mathbf{x}| = \sqrt{\sum_i x_i^2}$), and $\|\mathbf{M}\|$ to denote the Frobenius norm of a matrix \mathbf{M} ($\|\mathbf{M}\| = \sqrt{\sum_{ij} M_{ij}^2}$).

The least-squares minimization problem in Eq. (33) can be solved for the updated Jacobian $\mathbf{J}^{(m+1)}$ by setting $\partial S / \partial J_{ij}^{(m+1)} = 0$, which gives

$$\mathbf{J}^{(m+1)} = \mathbf{A}^{(m+1)} \times [\mathbf{B}^{(m+1)}]^{-1}, \quad (34)$$

where

$$\begin{aligned} \mathbf{A}^{(m+1)} &= w^{(0)} \mathbf{J}^{(0)} - \sum_{l=0}^m \Delta \mathbf{f}^{(l)} \otimes [\Delta \mathbf{x}^{(l)}]^\top, \\ \mathbf{B}^{(m+1)} &= w^{(0)} \mathbf{I} + \sum_{l=0}^m \Delta \mathbf{x}^{(l)} \otimes [\Delta \mathbf{x}^{(l)}]^\top. \end{aligned}$$

In the above equations \mathbf{I} denote the identity matrix.

In the limit where only the most recent iteration is used to update the Jacobian ($l = m$ in Eq. (33)) and $w^{(0)} \ll 1$, the VL method reduces to the Broyden-Fletcher-Goldfarb-Shanno (BFGS) Jacobian updating scheme.³⁸ We favor the VL method for its stability and efficiency, which will be illustrated in Sec. VI A.

By combining Eqs. (31) and (34) the constrained polarization calculation can be carried out, starting from a trial guess $\boldsymbol{\tau}^{(0)}$, $\boldsymbol{\mathcal{E}}^{(0)}$, and $\mathbf{J}^{(0)}$. At each step m of the algorithm, the electronic degrees of freedom are optimized by the minimization of the electric enthalpy in Eq. (2) at current atomic configuration $\boldsymbol{\tau}^{(m)}$ and electric field $\boldsymbol{\mathcal{E}}^{(m)}$. Subsequently, the Hellmann-Feynman forces $\mathbf{F}^{(m)}$ and polarization $\mathbf{P}^{(m)}$ are calculated using Eqs. (9) and (18), respectively. With them Eq. (31) can be formed, which gives the new $\boldsymbol{\tau}^{(m+1)}$ and $\boldsymbol{\mathcal{E}}^{(m+1)}$. Then $\mathbf{F}^{(m+1)}$ and $\mathbf{P}^{(m+1)}$ are re-evaluated at $(\boldsymbol{\tau}^{(m+1)}, \boldsymbol{\mathcal{E}}^{(m+1)})$, and the Jacobian is updated according to Eq. (34). The result, $\mathbf{J}^{(m+1)}$, is used to solve Eq. (31) in the next iteration of the algorithm, $m \leftarrow m + 1$. This refining procedure of $\boldsymbol{\tau}^{(m)}$ and $\boldsymbol{\mathcal{E}}^{(m)}$ continues until $\mathbf{F}^{(m)}$ and $\Delta \mathbf{P}^{(m)}$ both vanish. After convergence is reached, the algorithm moves to the next polarization constraint.

The Jacobian updating scheme in Eq. (34) requires an initial guess $\mathbf{J}^{(0)}$. It has to be set properly to assure reasonable step size during the first few optimization iterations. We construct $\mathbf{J}^{(0)}$ from a diagonal force-constant matrix $\mathbf{K}^{(0)} = k^{(0)} \mathbf{I}$, diagonal susceptibility tensor $\chi^{(0)} = \chi^{(0)} \mathbf{I}$, and Born effective charges equal to guessed static atomic charges $\mathbf{Z}^{(0)}$. The values of the $k^{(0)}$ and $\chi^{(0)}$ diagonal scaling factors and the elements of the $\mathbf{Z}^{(0)}$ matrix are the only free parameters of the algorithm, which makes it straightforward to use. There are certainly more sophisticated ways of initializing $\mathbf{J}^{(0)}$, for instance by using surrogate models,³⁹ e.g. force fields⁴⁰ combined with the polarizability model of Bilz et al.⁴¹ for the present purposes. However, this only matters during the first few relaxation steps of a new structure.

Moreover, if the calculation is to be done for multiple polarization target values, as is usually the case, the fully buildup \mathbf{J} -matrix can be passed from one calculation to the next and used as an initial guess to further improve the performance, as will be shown in Sec. VIA.

V. COMPUTATIONAL DETAILS

The method described in the previous sections has been implemented in our in-house version⁸ of the PARSEC open-source DFT code.⁴² We have applied it to study the ferroelectric properties of BaTiO₃ and PbTiO₃, as outlined below.

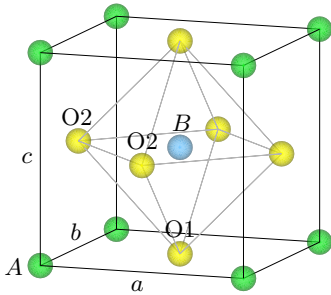


FIG. 1. Tetragonal unit cell of ABO_3 perovskite in the unsymmetrical phase. Atoms A, B, and O are represented by green, light blue, and yellow spheres, respectively. The symbols a , b , and c are the lattice constants. The labels next to the atoms indicate the positions of the atomic sites used to calculate the polarization quantum. The fractional coordinates, $(\frac{x}{a}, \frac{y}{b}, \frac{z}{c})$, of these locations are $(0, 0, 0)$ for A, $(0.5, 0.5, 0.5)$ for B, $(0.5, 0.5, 0.0)$ for O1, $(0.0, 0.5, 0.5)$ and $(0.5, 0.0, 0.5)$ for two equivalent O2 sites.

The unit cell of the considered perovskite compounds, with the formula ABO_3 , is depicted in Fig. 1. A tetragonal structure is assumed for both PbTiO₃ and BaTiO₃, which corresponds to their room temperature phase. The experimental lattice parameters used in this study are listed in Table I. The lattice is kept fixed during the calculations.

TABLE I. Experimental lattice parameters of the tetragonal perovskite structure of BaTiO₃⁴³ and PbTiO₃⁴⁴.

ABO_3	a, b [r_B]	c/a	Volume [r_B^3]
BaTiO ₃	7.53	1.01	431.69
PbTiO ₃	7.38	1.06	427.08

The atomic positions depicted in Fig. 1 are those of the centrosymmetric, non-polar reference state of ABO_3 perovskite oxides. The absolute values of the polarization components along the lattice vectors calculated for this paraelectric state are used to define the polarization quanta,²⁰ P_i^q , for a chosen unit cell. The actual values of the polarization, as reported in Sec. VI, are calculated

by subtracting P_i^q from the P_i values computed using Eq. (18), along the corresponding lattice vectors. This treatment allows to remove the “modulo $1/\Omega$ times real-space lattice vector” ambiguity⁴⁵ in the expression for \mathbf{P} in Eq. (18). The polarization calculated in this way is well-defined and independent of the choice of the unit cell. Note that this redefinition of \mathbf{P} agrees with the modern theory of polarization, which considers only the changes of the polarization with respect to a reference state.^{1–3}

In this work the pseudopotential model of a solid⁴⁶ is employed to describe the constituent atomic species. We utilize nonlocal norm-conserving ionic pseudopotentials cast in the real-space Kleinman-Bylander form,²⁶ to evaluate the interactions between the ion cores and the valence electrons. The pseudopotentials are generated with the `atom` software⁴⁷ and rely on the Troullier-Martins prescription.⁴⁸ Since this code only allows for one pseudized state per angular momentum channel, the semicore states of the Ba, Pb, and Ti atoms are kept in the core. Partial core correction⁴⁹ is included for these atoms in order to improve the quality of the solid-state calculations. The force term resulting from the use of a partial core correction is included into the calculations of the total forces acting on the Ba, Pb, and Ti atoms. This step is necessary due to the introduction of an explicit dependence of the exchange-correlation functional on atomic positions via the atom-centered core charge densities.⁵⁰

In the frozen-core approximation that underlies the pseudopotential theory, the species placed at the atomic sites are the effective ions. They are composed of the nucleus and the electron cores. For the chosen configurations of the pseudopotentials, the net positive charge of the nucleus plus core is: +2 for Ba, +4 for Pb, +4 for Ti, and +6 for O. These values of the atomic valence charges are used when evaluating the ionic polarization in Eq. (19) and forces due to the electric field in Eq. (26).

Within the pseudopotential approximation to DFT only the valence electrons are explicitly accounted for in the solid-state calculations. For the chosen valence-core partition the number of valence electrons per unit cell is $N = 24$ in the case of BaTiO₃ and $N = 26$ for PbTiO₃. In our implementation⁸ the valence electrons are represented by Wannier-like orbitals, which are calculated on uniform real-space grids spanning the localization regions (LRs). The wave functions are truncated beyond the LR boundaries. This is the only additional approximation as compared to standard real-space pseudopotential DFT calculations.⁵¹ The LR has a tetragonal shape and their size is determined by the multiple of unit cells, N_{cell} , that enter the LR. The positions of the LR are set at the beginning of the simulation and are kept fixed during the whole process. The number of LR is equal to the number of occupied orbitals. In the present work a double-occupancy of the orbitals is assumed. This implies that the $N = 24$ valence electrons in BaTiO₃ and $N = 26$ valence electrons in PbTiO₃ unit cells are covered

by $\frac{N}{2} = 12$ and $\frac{N}{2} = 13$ orbitals, respectively. In both compounds the LRs for 12 of these orbitals are centered on the O1 and O2 sites shown in Fig. 1. The 4 orbitals per O atom site are initialized with Gaussians having a s , p_x , p_y , and p_z symmetry, and an origin on the central O atom. The additional orbital in PbTiO_3 is calculated in a LR centered on the Pb atom located at the A site in Fig. 1. The initial guess for this orbital is taken to be a spherically symmetric Gaussian function.

Before proceeding, we should acknowledge an additional theoretical subtlety associated with the correct choice of the exchange-correlation functional in the electric-field problem. The currently accepted view^{52–54} is that a dependence on the polarization should be present in the exchange-correlation functional — leading to a density-polarization functional theory. However, no realistic polarization-dependent functional has been proposed yet and in this work we remain at the standard LDA level. We use the exchange-correlation functional of Ceperley and Alder,⁵⁵ as parameterized by Perdew and Zunger.⁵⁶

VI. RESULTS

In this section, the computational scheme outlined above is illustrated by applying it to a series of problems involving constrained polarization calculations in tetragonal perovskite compounds. First, the accuracy of the calculations is verified and the performance of the optimization algorithm is examined. Then, results concerned with the ferroelectric behavior of BaTiO_3 and PbTiO_3 are presented and the differences in the ferroelectric properties between the materials are studied.

A. Numerical tests

The reliability of structural relaxation calculations is determined by the accuracy of the atomic forces. Directly solving for localized orbitals by constraining the wave functions to be zero outside the localization regions (LRs) introduces an error in the total energy,⁵⁷ which is expected to be present in the case of forces too. It has been shown by the authors in Ref. 8 that the errors due to the localization constraint can be alleviated by allowing the localized wave functions to be non-orthogonal, what leads to non-orthogonal generalized Wannier functions (NGWFs). In particular, it has been demonstrated that total energy calculations in the presence of electric field converge faster with increasing LRs size when using NGWFs instead of orthogonal Wannier functions (WFs).

The study carried out in Ref. 8 considered clamped atoms in their equilibrium structure. In Fig. 2 we show how the localization error affects the total forces induced by the atomic distortion. The off-equilibrium structure results from a displacement of the Ti atom from its centrosymmetric position in Fig. 1 by $\Delta_z = 0.1 \times c$. The

quantity plotted in Fig. 2 is the relative deviation of the forces computed with NGWFs and WFs from the values obtained using Bloch functions, which are taken to be a converged result. In this case Brillouin zone integrations are performed on a $3 \times 3 \times 3$ Monkhorst-Pack mesh⁵⁸ and the pseudopotential force terms are calculated in a standard way, from the derivatives of the ionic potentials²⁷. We note that thanks to the improved numerical accuracy of the alternative force formulas in Eqs. (23) and (25), when discretized on the real-space grid, a coarser grid can be used to obtain the forces appropriately converged with respect to the grid spacing. The grid step required to converge the forces is $0.3a$ and $0.15a$ when using the alternative and standard scheme to calculate the pseudopotential forces, respectively. Hence, the number of required grid points decreases by a factor of 8 to represent each wave function.

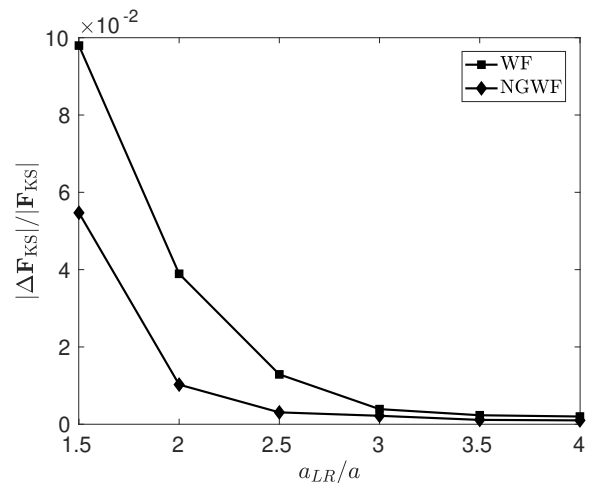


FIG. 2. Convergence of atomic forces as a function of the LR size in tetragonal BaTiO_3 at a fixed, off-equilibrium geometry. The forces are induced by displacing the Ti atom in the centrosymmetric structure of Fig. 1 by $\Delta_z = 0.1 \times c$. \mathbf{F} is the force vector calculated with localized orbitals, either NGWFs (line with diamonds) or WFs (line with squares). The reference forces \mathbf{F}^{ref} were obtained using Bloch functions.

Figure 2 shows that the error in forces goes to zero with increasing LRs size, as expected. We also see that the error decays much faster for NGWFs than WFs. The convergence of forces with respect to the LR size is somewhat slower than that of the total energy and polarization. It thus determines the overall accuracy of the calculations. As can be seen in Fig. 2, the forces obtained from NGWFs are already in good agreement with the reference result, with no localization constraint, setting $a_{LR} = 2.5a$. In this case the relative deviation is less than 0.3%. For the forces calculated with WFs $a_{LR} = 3.5a$ is required to reach a similar accuracy. This amounts to a volume difference by a factor of 2.7 to represent each wave function.

The efficiency of our method for performing constrained polarization calculations in the case of tetrag-

onal BaTiO₃ is illustrated in Fig. 3. The starting configuration for the subsequent simulations is the centrosymmetric perovskite structure in Fig. 1, under zero electric field. The required polarization constraints P_t are aligned with the c axis. The initial Jacobian $\mathbf{J}^{(0)}$ is set according to the prescription given in Sec. IV, with a diagonal force constant matrix formed from $k^{(0)} = 0.1$, a diagonal susceptibility tensor scaled by $\chi^{(0)} = 5.0$, and Born effective charges substituted by nominal valences +2 for Ba, +2 for Pb, +4 for Ti, and -2 for O. The weight associated with $\mathbf{J}^{(0)}$ is $w^{(0)} = 0.01$ and the information from all previous iterations is incorporated when evaluating the Jacobian update according to Eq. (34). The \mathbf{J} -matrix is carried over from one converged relaxation to the next. The convergence criterion is such that the forces are smaller than $10^{-3}\text{Ry}/r_B$, and the polarization fulfills the constraint by at least $10^{-5}r_B^{-2}$.

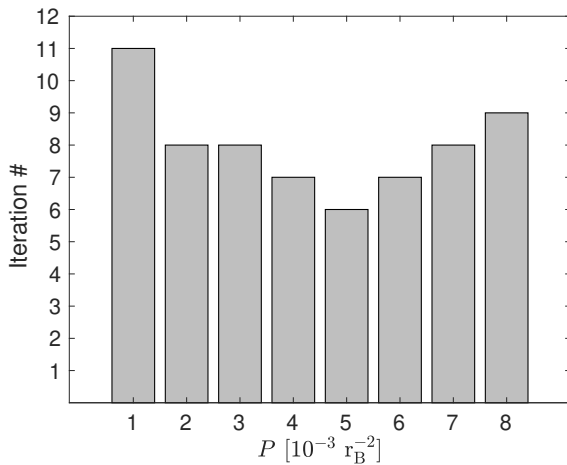


FIG. 3. Number of iterations required to converge the quasi-Newton algorithm for constrained polarization calculations in tetragonal BaTiO₃. Starting from the centrosymmetric perovskite structure under zero electric field conditions calculations at consecutive polarization constraints P_t are performed. The solution variables and the Jacobian are carried over from one calculation to the next. In the first one the $\mathbf{J}^{(0)}$ matrix from Sec. IV is used to initialize the Jacobian.

There are six degrees of freedom to optimize in the calculations. They consist of the internal z coordinates of five atoms in the perovskite unit cell and the electric field component along the c axis. It is thus a good example to show the performance of our method, because there are enough degrees of freedom to make a direct minimization impractical. As can be seen in Fig. 3 the convergence of our method is achieved after 6 to 11 iterations for all considered polarization constraints, which, as will be shown in Sec. VIB, are sufficient to extract the energy landscape of tetragonal BaTiO₃. The increased number of iterations in the first configuration, at $P_t = 1 \times 10^{-3} r_B^{-2}$, as compared to the following ones, is due to the fact that the $\mathbf{J}^{(0)}$ matrix is used to start the iteration. In the next cases a better initial guess for the Jacobian can be

employed, taken from a fully built-up \mathbf{J} -matrix resulting from the previous polarization constraint. Another noticeable feature of the convergence behavior of the algorithm is the decreased number of iterations in the vicinity of $P_t = 5 \times 10^{-3} r_B^{-2}$: this polarization constraint is close to the minimum of the potential energy well. As a consequence, the harmonic approximation leading to the quasi-Newton step in Eq. (31) is best fulfilled around this point.

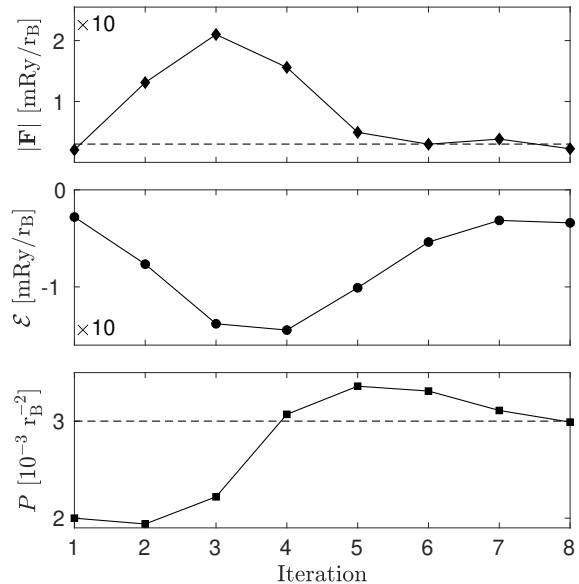


FIG. 4. Relaxation of tetragonal BaTiO₃ at $P_t = 3 \times 10^{-3} r_B^{-2}$. The starting configuration and the initial Jacobian are taken from a converged calculation at $P_t = 2 \times 10^{-3} r_B^{-2}$. Top panel: L^2 -norm of the forces acting on the atoms. Middle panel: electric field component along the c axis. Bottom panel: polarization along \mathcal{E} . The convergence threshold for the forces and the polarization constraint are indicated by the dashed lines in the top and bottom panels, respectively.

As an example of the algorithm functionality, Fig. 4 shows the convergence of the L^2 -norm of all calculated forces, together with the evolution of the electric field and polarization as a function of the number of iterations. This numerical experiment corresponds to going from a polarization constraint of $P_t = 2 \times 10^{-3} r_B^{-2}$ to $P_t = 3 \times 10^{-3} r_B^{-2}$. During the first iterations the electric field increases in magnitude due to the difference between the polarization value and the constraint. Note the correct direction of change of the electric field and the polarization from the first iteration. This feature can be attributed to the correct information about the electric enthalpy surface contained in the \mathbf{J} -matrix carried over from the previous calculation. The change in the electric field induces the forces responsible for moving the atoms.

The relaxation proceeds by displacing the atoms and adjusting the electric field so that the atomic forces are balanced and the polarization constraint is simultaneously satisfied.

B. Ferroelectricity in tetragonal BaTiO₃

Having verified the convergence of our method, we now demonstrate its utility by analyzing the energy landscape of tetragonal BaTiO₃. Figure 5 shows the calculated cross section of the potential energy surface as a function of the polarization along the c axis. The electric field component along the same axis, which is required to realize the polarization states, is also plotted in Fig. 5. As can be seen, the minimum of the energy is at non-zero value of P . This is the typical signature of ferroelectricity. This minimum coincides with the zero-crossing of \mathcal{E} and corresponds to the equilibrium state of the material. The value of the spontaneous polarization at this point, $P_s = 5 \times 10^{-3} \text{ r}_B^{-2}$, in SI units, can be converted to 0.286 C/m^2 and agrees well with the experimental value⁵⁹ of 0.26 C/m^2 . For $P > P_s$ the state can be realized by applying an appropriate fixed electric field $\mathcal{E} > 0$. The states with $P < P_s$ and $\mathcal{E} < 0$ are local maxima of the electric enthalpy and thus cannot be reached by a direct application of the electric field. It has been recently proposed that ferroelectric materials can be biased into the $\{P < P_s, \mathcal{E} < 0\}$ state by putting them in series with a dielectric⁶⁰. In this case \mathcal{E} acts as a depolarizing field due to the incomplete screening of the ferroelectric polarization.

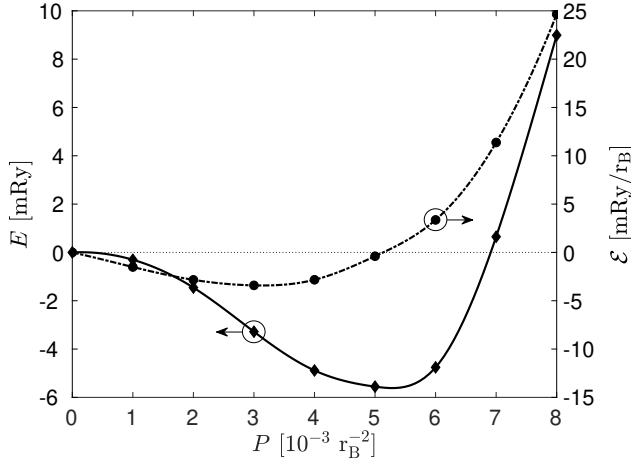


FIG. 5. Calculated energy (diamonds) and electric-field (circles) as a function of the polarization in tetragonal BaTiO₃. The energy E is the Kohn-Sham total energy in Eq. (17) per 5-atom unit cell. The electric field \mathcal{E} is aligned with the c axis and imposes the polarization argument P along the same axis.

In addition to the physical consistency of our results we also report a good agreement between our cal-

culated potential energy curve and the one obtained by DV in Ref. 12. DV found the energy minimum to be located at $P_s = (5 \pm 0.1) \times 10^{-3} \text{ r}_B^{-2}$ with a well depth $E_{\min} = (6 \pm 0.1) \text{ mRy}$. Similarly, in our calculations the absolute value of the energy minimum at $P_s = 5 \times 10^{-3} \text{ r}_B^{-2}$ is $E_{\min} = 5.56 \text{ mRy}$. Given the difference in the pseudopotentials used and our choice of the lattice parameter, it cannot be excluded that, this level of agreement is partly fortuitous as the ferroelectric potential energy surfaces are quite sensitive to the choice of the lattice constant and to the approximations in first-principles calculations. Furthermore, different methods are used in Ref. 12 and here.

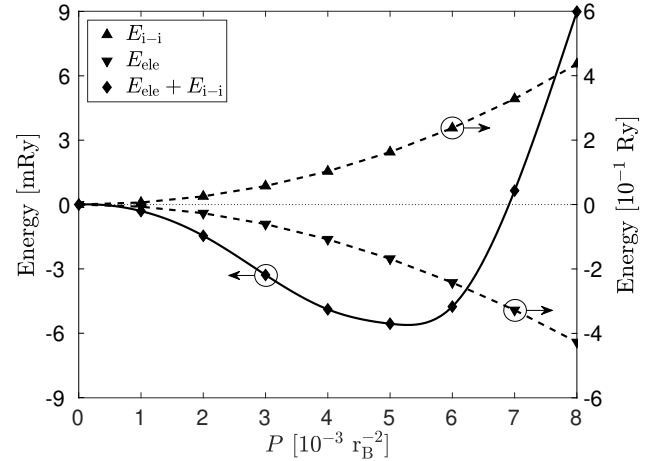


FIG. 6. Decomposition of the total energy in BaTiO₃ into the electronic and ion-ion terms. The electronic energy E_{ele} is the band-structure term minus double-count corrections. The component E_{i-i} is the Ewald energy among the ion cores. The sum $E_{\text{ele}} + E_{i-i}$ is the total Kohn-Sham energy in Eq. (17).

In order to make a better understanding of the BaTiO₃ energy landscape, in Fig. 6 we have decomposed the total energy into its electronic and ion-ion interaction contributions. It is notable from this figure that the ion-ion repulsion energy increases with P , whereas the electronic energy decreases. The lowering of the electronic energy can be related to the process of covalent bond formation (hybridization), what will be shown later in this section. The total energy is the sum of both contributions. As can be deduced from Fig. 6, in order to produce a ferroelectric potential well, the electronic energy must decrease faster than the ion-ion energy increases for $P < P_s$. Thus, if the hybridization processes are not strong enough the ferroelectric state is not stabilized. For $P > P_s$ the short-range repulsions start to dominate and consequently the total energy increases with P .

The variation of the total energy is due to atomic displacements and the changes in the electronic structure. Figure 7 shows the polarization dependence of the atomic coordinates in BaTiO₃ for tetragonal distortions along the c axis. The atomic displacement pattern displayed in Fig. 7 is such that the O1 and

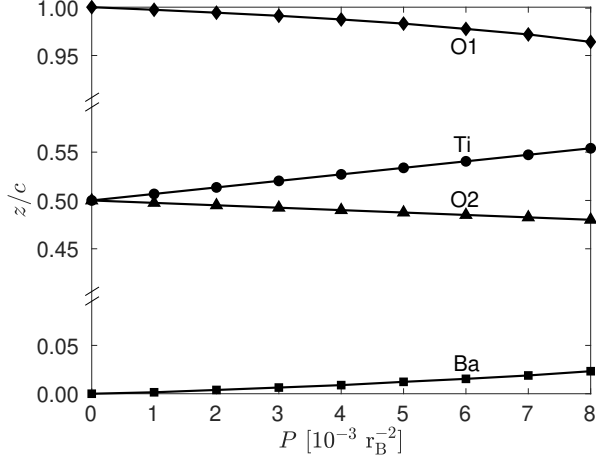


FIG. 7. Internal z coordinates for each atom in BaTiO_3 unit cell as a function of polarization P along the c axis. For initial atomic positions, at $P = 0$, see Fig. 1. Top-most points (diamonds) correspond to translational image of O1 atom in neighboring unit cell. The coordinates at $P = 5 \times 10^{-3} \text{ r}_B^{-2}$ give the equilibrium positions of the atoms.

O2 atoms move downward, in a direction opposite to the Ba and Ti atoms, which move upward with increasing P . For $P \leq P_s$ the atoms listed in order of increasing displacements from the initial positions are $\{\text{Ba}, \text{O2}, \text{O1}, \text{Ti}\}$. This sequence changes for $P > P_s$ as the magnitude of the Ba displacement exceeds that of O2, changing the character of the structural distortion. At $P = P_s$ the fractional displacements of Ti, O1, and O2 atoms with respect to Ba ($\frac{\Delta_z(\text{Ti})}{c}, \frac{\Delta_z(\text{O1})}{c}, \frac{\Delta_z(\text{O2})}{c}$)_{Ba} are found to be $(0.019, -0.029, -0.023)$. The calculated values in the equilibrium state are in good overall agreement with the experimentally measured displacements⁴³ $(0.015, -0.023, -0.014)$. As can be seen, the displacement pattern is preserved between the calculated and experimental tetragonal distortions. This finding is consistent with the results of standard structural relaxations within DFT and LDA at experimental lattice parameters, which predict equilibrium displacements⁶¹ $(0.013, -0.025, -0.016)$, in agreement with our results at $P = P_s$.

The atomic movement induce the electronic charge redistribution. This results in the displacement of the centroids of charge of the orbitals (OCs). As for the orbitals initially centered on the O2 atomic sites, we observe that the OCs of 4 orbitals per each O2 atom follow it when moving. On average, a charge of -8 electrons (due to the double occupancy of the orbitals) moves together with the $+6$ point charge of the O ion so that it can be effectively treated as an anion carrying -2 charge. Hence, when the O2 atom is displaced in the negative direction along the coordinate axis, as in Fig. 7, it gives rise to a positive contribution to the total polarization.

The situation is more interesting for the O1 orbitals, centered initially on the O1 atomic site. The displace-

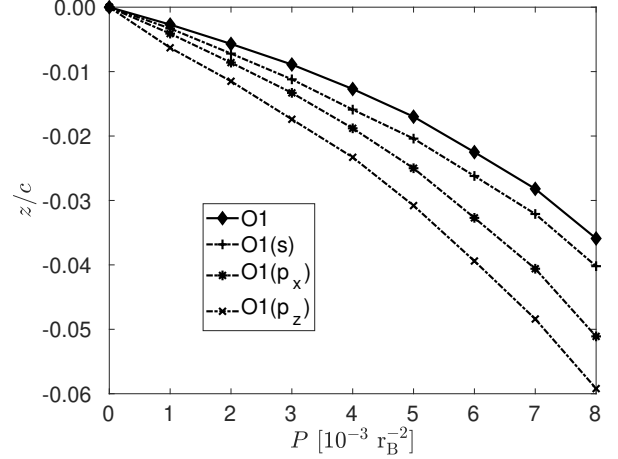


FIG. 8. Computed z coordinate of the O1 orbitals centroids of charge (dashed lines) and of O1 atom (solid line) in BaTiO_3 as a function of the polarization P along the c axis. The orbitals are labeled by their dominant atomic character on the O1 atom. The coordinates of $\text{O1}(p_y)$ OC overlap with those of $\text{O1}(p_x)$ OC.

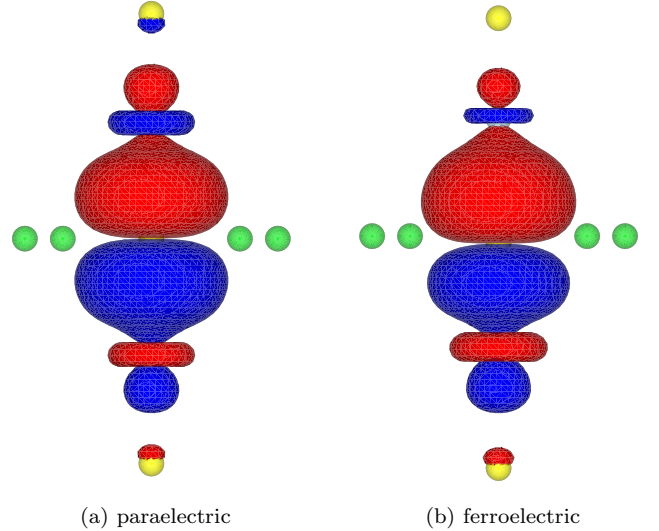


FIG. 9 (Color online). Amplitude isosurface plots of the $\text{O1}(p_z)$ WFs in BaTiO_3 at $\pm 0.015 \text{ r}_B^{-3/2}$. Red and blue surfaces correspond to positive and negative amplitudes, respectively. The orbitals are oriented along the O–Ti–O–Ti–O chains. O is at the center, embedded in the p_z atomic orbital; above and below are the Ti atoms (light blue), almost hidden under the d_{z^2} orbitals; the two other O atoms (yellow) are located at the top and bottom. The four Ba atoms (light green) neighboring the central oxygen are also shown. (a) Paraelectric state at $P = 0$. (b) Ferroelectric state at $P = P_s$.

ments along the c axis of the computed OCs for these orbitals are plotted as a function of P in Fig. 8. The labeling of the orbitals is according to the dominant atomic character on the O1 site in the centrosymmetric structure. The displacement of the O1 atom is also shown for reference. As it can be observed, when the O1 atom moves in the $-z$ direction, the OCs of the O1 orbitals are displaced downward, even more than the O1 atom has moved. The shift of the O1 OCs is towards Ti atom, which moves upward, in the direction of the O1 atom (see Fig. 7). This relative displacement of the O1 OCs with respect to the moving atoms leads to a larger positive contribution to the total polarization than if the O1 OCs would move rigidly with the O1 ion. To investigate the physical processes modulating the amplitude of the O1 OCs displacement, which enhance the electronic polarization, we will now visualize the O1 orbitals and study their transformations induced by the atomic displacement.

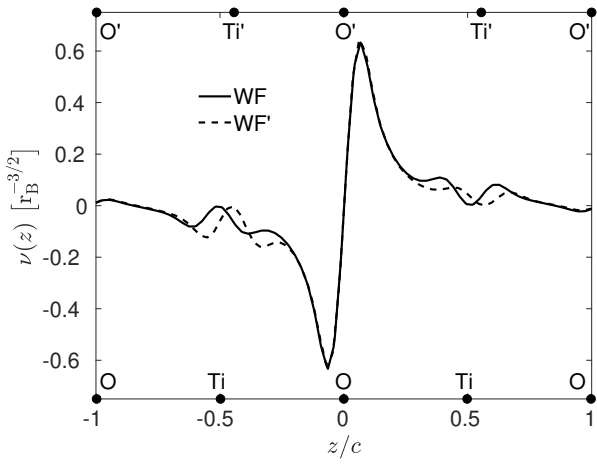


FIG. 10. Line plot along the $[001]$ direction of $O1(p_z)$ WFs in the paraelectric and ferroelectric states of $BaTiO_3$. The z coordinate is with respect to the O atom in the center. The positions of the atoms in the paraelectric and ferroelectric states are depicted at the bottom and top axes, respectively.

Figure 9 displays the changes of the $O1(p_z)$ WF going from a paraelectric phase ($P = 0$) to the ferroelectric equilibrium state ($P = P_s$). As evidenced by Fig. 9a, this orbital clearly shows a hybridization between the Oxygen p_z atomic orbital in the center of the figure and the d_{z^2} atomic orbitals on the neighboring Ti atoms. It thus forms a σ -type of bond oriented along the Ti–O–Ti chain. This bonding changes in the ferroelectric state, as shown in Fig. 9b. Compared to the paraelectric state, the hybridization strengthens for the lower O–Ti bond and weakens for the upper one. These modifications of the chemical bonding are due to electronic charge transfers induced by the atomic displacement.

To better visualize this process, we plot in Fig 10 the overlaid cross-sections of the $O1(p_z)$ WF along the O–Ti–O–Ti–O atomic chains in the paraelectric and ferro-

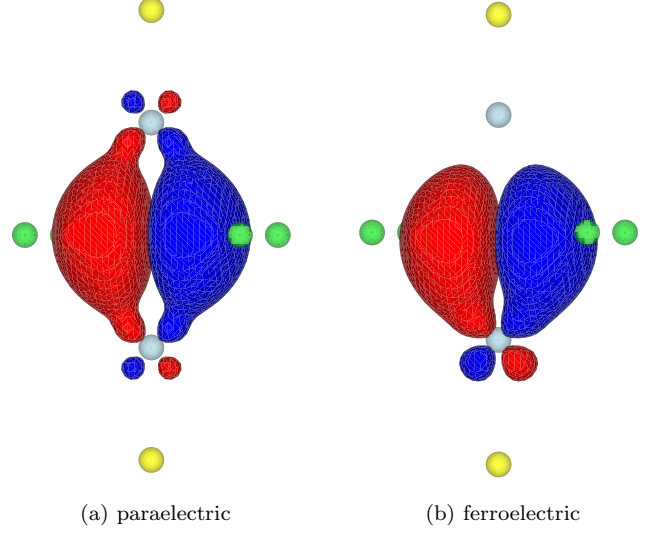


FIG. 11 (Color online). Amplitude isosurface plots of the $O1(p_x)$ WFs in $BaTiO_3$ at $0.02 r_B^{-3/2}$. (a) Paraelectric state at $P = 0$. (b) Ferroelectric state at $P = P_s$. For the location of the atoms and the color scheme, see Fig. 9.

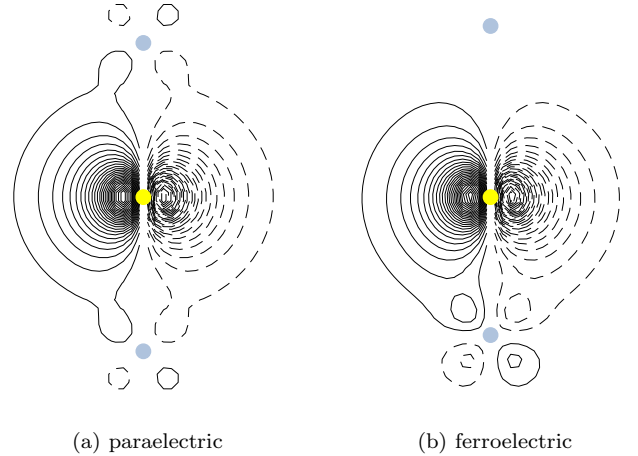


FIG. 12 (Color online). Contour plots in the (020) plane of the $O1(p_x)$ WFs in $BaTiO_3$. The contour intervals are $0.02 r_B^{-3/2}$.

electric states. The amplitude of the orbital wave function increases in the ferroelectric state around the left Ti atom, which is displaced from its initial position at $z = -0.5c$ towards the O atom in the center. This happens at the expense of the wave function around the right Ti atom, initially at $z = 0.5c$, which moves apart from the central O atom and whose amplitude decreases. Consequently, the hybridization to the Ti d_{z^2} states strengthens for shortened bond (Fig. 9 bottom), giving it a more covalent character, and weakens for the elongated one (Fig. 9 top), resulting in a more ionic-like bond. Note that the central part of the wave function does not change

when the atoms move and retains its p_z shape around the central O atom. Thus, it can be concluded that the charge redistribution of the $O1(p_z)$ orbital, as induced by the atomic displacement, is non-local and due to off-site changes of hybridization at the neighboring Ti atoms. The transfer of charge between the Ti atoms results in the displacement of the $O1(p_z)$ orbital centroid of charge, giving rise to electronic polarization.

A similar conclusion can be drawn by analyzing the transformations of the $O1(p_x)$ and $O1(p_y)$ WFs. These orbitals form π -type bonds between the O and its neighboring Ti atoms, as shown in Fig. 11 for the $O1(p_x)$ WF. The form of the displayed wave function in the paraelectric state, Fig 11a, clearly shows the hybridization between the p_x atomic orbital on the O atom in the center and the d_{xy} atomic orbitals on the neighboring Ti. This hybridization significantly changes in the ferroelectric state. As can be seen in Fig. 11b the admixing of Ti d_{xy} contribution to the Wannier function gets much stronger for the bottom Ti atom, while it almost disappears for the top one. At the same time the bulk part of the wave function in the form of a p_x orbital on the central O atom remains unchanged under the ferroelectric distortion. This can be better visualized in Fig. 12 which plots the contours of the $O1(p_x)$ WFs projected onto the (020) plane passing through the Ti–O–Ti chain along the [001] axis parallel to the plane. As is apparent from this figure, the transfer of charge takes place from the upper to the lower Ti atom, leaving the central part of the wave function unaffected. Hence, similarly as for the $O1(p_z)$ orbital, the mechanism responsible for the anomalous displacement of the $O1(p_x)$ orbital centroid of charge induced by the ferroelectric atomic distortion is identified to be an interatomic transfer of charge between neighboring Ti atoms due to modified hybridizations.

The hybridization between the p orbitals of O and d orbitals of Ti in BaTiO_3 is a well-known feature, confirmed by various sources: experiments,^{62,63} calculations based on linear combination of atomic orbitals (LCAO),^{64–66} and DFT results.^{14,37} Within the framework of DFT, Cohen and Krakauer¹⁴ deduced the increased hybridization between the O $2p$ and O $3d$ states caused by the ferroelectric distortion by analyzing the densities-of-states in tetragonal BaTiO_3 at experimental atomic displacements. Marzari and Vanderbilt³⁷ obtained maximally localized Wannier functions (MLWFs) in cubic BaTiO_3 from the postprocessing step after a conventional electronic-structure calculation. Changes in hybridization were illustrated by manually displacing the Ti atom along the Ti–O bond. It is worth mentioning that the qualitative features of MLWFs are similar to our WFs. However, at variance with other approaches our method allows to directly inspect the changes in hybridization and at the same time correlate it with the underlying energetics as the localized orbitals are obtained by the requirement of the energy minimum.

C. Enhanced ferroelectricity in tetragonal PbTiO_3

In this section, we use our approach to study the ferroelectricity of tetragonal PbTiO_3 . The obtained results are compared to those of BaTiO_3 , discussed in the previous section, to highlight the differences between both compounds.

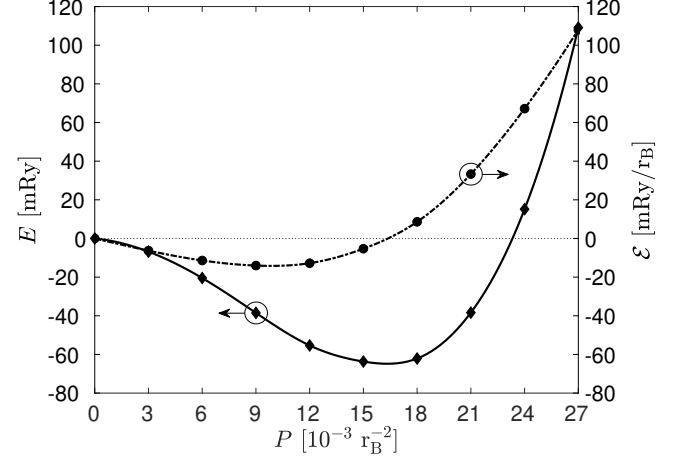


FIG. 13. Computed energy (diamonds) and electric-field (circles) as a function of the polarization for tetragonal PbTiO_3 . The Kohn-Sham total energy E is per 5-atom unit cell. The electric field \mathcal{E} and the polarization P are the non-zero components along the c axis.

The calculated potential energy $E(P)$ curve and the values of the \mathcal{E} -field along the c axis that are required to impose the polarization constraint in tetragonal PbTiO_3 are plotted in Fig. 13. Our calculations show that this compound stabilizes at a larger value of the spontaneous polarization, $P_s = 15 \times 10^{-3} r_B^{-2}$, and with a deeper potential energy well, $E_{\min} = 63.7 \text{ mRy}$, as compared to BaTiO_3 . The larger derivatives of E with respect to P in the case of PbTiO_3 results in higher values of the electric field, as expected from Eq. (1). Similarly to BaTiO_3 , the zero-crossing of \mathcal{E} corresponds to the minimum location of E , thus verifying the internal consistency of the results. The extracted value of P_s for PbTiO_3 in SI units is 0.86 C/m^2 , which agrees reasonably well with the experimental value⁶⁷ 0.75 C/m^2 . Since a similar conclusion was drawn for BaTiO_3 , this gives a first hint about the well captured relative ferroelectric behavior of BaTiO_3 and PbTiO_3 in our calculations. Another confirmation is provided by the large difference between the calculated well depths of BaTiO_3 and PbTiO_3 , which was also reported in previous DFT studies^{14,68} using experimental atomic displacements to investigate the potential energy surfaces of these materials.

Figure 14 shows that the greater potential energy well depth for PbTiO_3 is due to enhanced electronic processes, which give rise to a lowering of the electronic energy and help to stabilize the ferroelectric state at larger spon-

taneous polarization relative to BaTiO₃. This result also implies that the hybridization processes should be stronger in the case of PbTiO₃, a point that will be confirmed in the following.

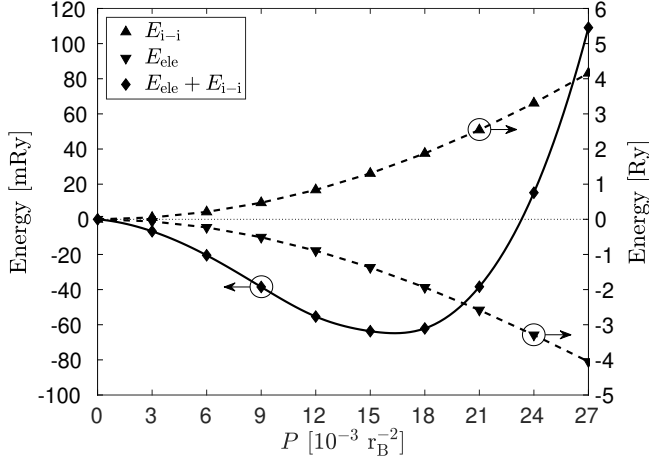


FIG. 14. Decomposition of the total energy in PbTiO₃ into the electronic, E_{ele} , and ion-ion, E_{i-i} , terms.

The large polarization in PbTiO₃ is correlated with the substantial atomic distortions displayed in Fig. 15. As can be seen, the pattern resembles that of BaTiO₃, for greater overall magnitudes of the displacements of the corresponding atoms. A more detailed analysis of the structural distortions reveals however that the ordering of the atoms according to the magnitude of their displacements with respect to their initial positions is actually reversed in PbTiO₃ as compared to BaTiO₃, i.e. {Ti, O1, O2, Pb} instead of {Ba, O2, Ti, O1}. This result is supported by experimental data. The measured fractional displacements of the Ti, O1, and O2 atoms with respect to Pb, are⁴⁴ $(-0.049, -0.117, -0.120)$, whereas those extracted from our calculations at P_s are $(-0.052, -0.147, -0.152)$. Both simulation and experiment show that in PbTiO₃ the displacement of O2 towards Pb is greater than that of O1 towards Ti, while in BaTiO₃ the situation is the opposite as the O2–Ba displacement is smaller than the O1–Ti movement (see previous section). Thus, the difference in the character of the structural distortion between BaTiO₃ and PbTiO₃ is well reproduced by our calculations.

In order to clarify the microscopic mechanism leading to large stabilized ferroelectric polarization in PbTiO₃ relative to BaTiO₃ we will now turn to the inspection of the PbTiO₃ WFs and compare the electronic structures of both materials.

The O2 orbitals in PbTiO₃ respond to the atomic distortions alike the corresponding orbitals in BaTiO₃. The relative displacement of the OCs centered initially on the O2 atomic sites is negligible when the O2 atoms move. An average of -8 electron charges can be associated with each O2 site. Summed up with the $+6$ charge of the O

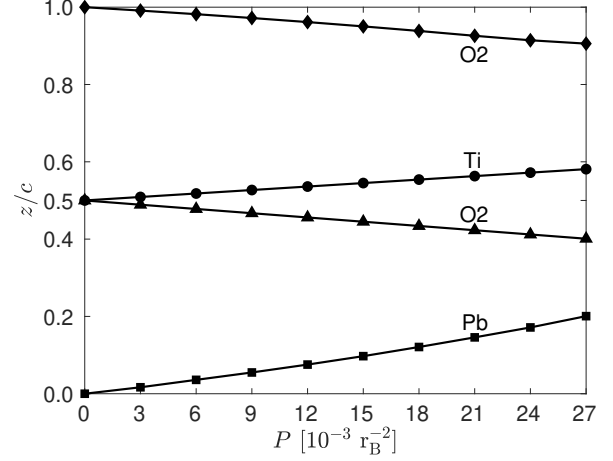


FIG. 15. Internal z coordinate of each atom in the PbTiO₃ unit cell as a function of the polarization P along the c axis. The coordinates at $P = 15 \times 10^{-3} \text{ r}_B^{-2}$ correspond to the equilibrium positions of the atoms.

ion this gives a -2 effective charge contribution to the total polarization coming from the displacement of the O2 atoms, as in BaTiO₃.

The larger stabilized polarization of PbTiO₃ can be partially attributed to the greater relative displacements of the O1 OCs with respect to the O1 atom. The movement of the O1 OCs and of the O1 atom along the c axis is displayed in Fig. 16. By comparing it to Fig. 8, which plots the corresponding data for BaTiO₃, it is evident that the relative displacements of the O1 OCs with respect to the O1 atom towards the Ti atom, are more significant in PbTiO₃ than in BaTiO₃. As a consequence a larger positive contribution to the electronic polariza-

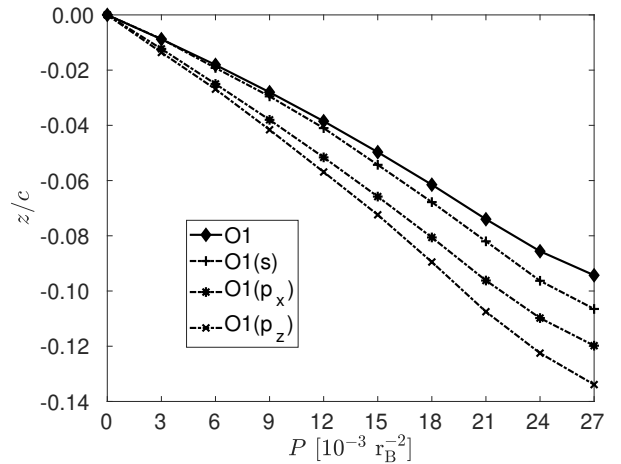


FIG. 16. Computed z coordinate of the O1 OCs (dashed lines) and of the O1 atom (solid line) in PbTiO₃ as a function of the polarization P along the c axis. The coordinates of the O1(p_y) OC overlap with those of the O1(p_x) OC.

tion comes from these orbitals in PbTiO_3 . A possible explanation is given by the stronger hybridization between the O and Ti atomic orbitals in this compound. We find that the character of the hybridization is the same as in BaTiO_3 . It is related to interatomic transfer of charge between the neighboring Ti atoms. The difference in the displacement of the O1 OCs and the related contribution to the electronic polarization come from the stronger amplitudes of these processes in PbTiO_3 than in BaTiO_3 .

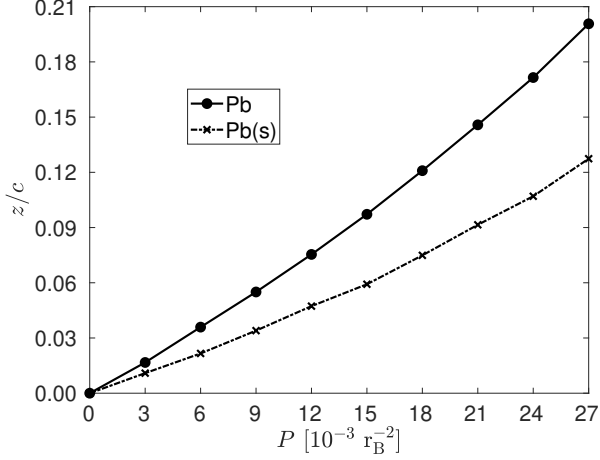


FIG. 17. Computed z coordinate of the $\text{Pb}(s)$ OC (dashed lines) and of the Pb atom (solid line) in PbTiO_3 as a function of the polarization P along the c axis.

Another reason behind the relatively large polarization of PbTiO_3 is the presence of the Pb lone electron pair. In our calculations these electrons are represented by a doubly-occupied WF, which in the centrosymmetric structure is centered on the Pb atom and displays a dominant atomic s character. It is thus labeled as $\text{Pb}(s)$. The displacement of the $\text{Pb}(s)$ OC as a function of the polarization along the c axis is shown in Fig. 17. As can be seen, the $\text{Pb}(s)$ OC lags behind the moving Pb atom. This leads to a larger positive contribution to the total polarization than if the $\text{Pb}(s)$ orbital would rigidly follow the Pb atom. In a purely ionic picture, where the Pb electrons remain centered on the Pb atom when moving, the contribution to the total polarization coming from the displacement of the Pb ion would be +2 point charges, as the Ba ion in BaTiO_3 . This is not the case in PbTiO_3 . Since the center of charge of the $\text{Pb}(s)$ orbital is displaced downward with respect to the moving upward Pb, the positive charge of the Pb ion is exposed and a larger positive contribution to the total polarization than in a purely ionic scenario is obtained.

The mechanism responsible for the enlarged polarization contribution of the Pb atom, relative to its nominal ionic charge, resembles a local electronic polarizability at the Pb site, as displayed in Fig. 18. In contrary to the O1 orbitals, the $\text{Pb}(s)$ shell charge entirely moves with respect to the Pb atom when transforming from the para-

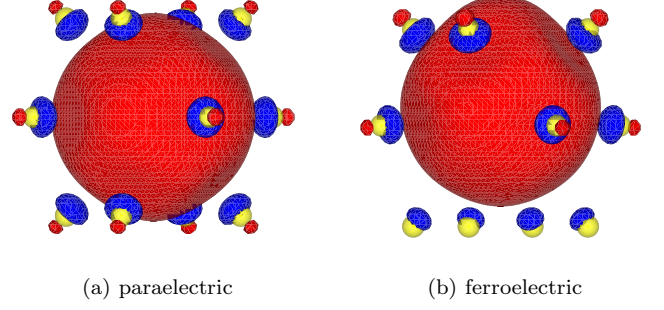


FIG. 18 (Color online). Amplitude isosurface plots of the $\text{Pb}(s)$ WFs in PbTiO_3 at $\pm 0.015 r_B^{-3/2}$. The red and blue surfaces correspond to positive and negative amplitudes, respectively. Pb is at the center, hidden under an s atomic orbital, surrounded by 12 O atoms (yellow). (a) Paraelectric state at $P = 0$. (b) Ferroelectric state at $P = P_s$.

electric to the ferroelectric state. This behavior is evident in Fig. 19. The charge redistribution of the $\text{Pb}(s)$ orbital in response to the atomic displacement is attributed to its interactions with the neighboring O atoms. It can easily be seen in Fig. 18 that, in addition to the distinctive atomic s orbital on the central Pb site, there are significant sp -like contributions sitting on the 12 neighboring oxygens. This supports the postulate that Pb in PbTiO_3 has a non-negligible covalent character.¹⁴ In the ferroelectric state the Pb–O hybridization increases for the upper O atoms and decreases for the lower ones, resulting in interatomic charge transfers. However, the dominant mechanism driving the shift of the $\text{Pb}(s)$ OC with respect to Pb atom is the on-site orbital reorganization following the change in the underlying crystal potential. The later is caused by the relative displacements of Pb and O atoms.

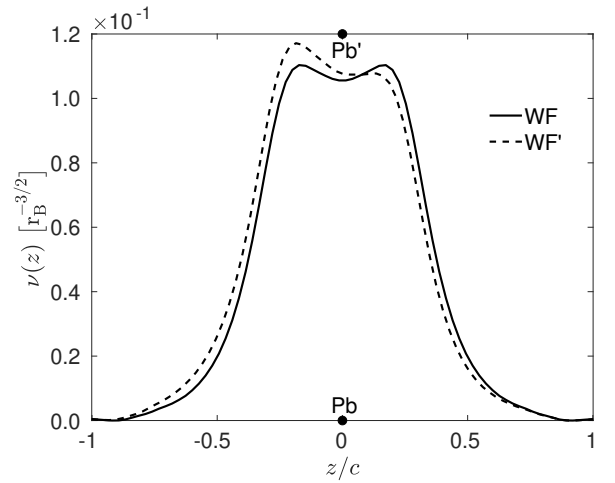


FIG. 19. Line plot along the $[001]$ direction of the $\text{Pb}(s)$ WFs in the paraelectric and ferroelectric states of PbTiO_3 . The z coordinate is defined with respect to the Pb atom in the center.

The hybridization between the Pb s and O p states seems to indirectly influence the Ti–O interactions, which are mainly responsible for the ferroelectricity in both studied perovskite compounds. In addition, the favorable interactions between Pb and O cause the energy to be lowered if the Pb–O2 distance is reduced. This leads to the conclusion that it is the hybridization between Pb and O and the greater interactions between Ti and O that cause the larger polarization and greater well depths of PbTiO₃.

VII. CONCLUSION

We have presented a formalism to perform first-principles calculations of insulators at fixed polarization. The approach has been implemented within the DFT framework into a practical computational scheme that allows to find the most stable electronic and structural configuration of an insulating crystal when its electric polarization is constrained to a given value. The method has been applied to obtain the $E(\mathbf{P})$ curves for two paradigmatic ferroelectric materials, BaTiO₃ and PbTiO₃ in

their tetragonal phase.

In addition to qualitative results, the Wannier-function-based description of the electronic structure of our approach yields a meaningful picture in real-space of the flow of electronic charge in terms of bonding. It has been demonstrated how a careful analysis of the Wannier functions can shed light on relevant physics concerning the electronic polarization of perovskites. Two different basic mechanisms of electronic polarization, interatomic charge transfers and local polarizability, have been visualized and associated with ferroelectric transformations.

The comparative study of BaTiO₃ and PbTiO₃ using our approach has enabled us to clarify the special role of Pb at the A-site. The presence of a Pb lone electron pair causes a strong covalency between Pb and O, resulting in larger polarization in PbTiO₃ as compared to BaTiO₃. Hybridization between Pb-cation also leads to increased Ti–O interactions which further stabilize the ferroelectric state. In both compounds the Ti–O hybridization is crucial to allow for ferroelectricity. With the help of localized Wannier functions these processes can be directly inspected and quantified by examining the relative displacements of the centroids of charge of the orbitals with respect to the moving atoms at fixed polarization.

-
- * pawell@iis.ee.ethz.ch
- ¹ R. D. King-Smith and D. Vanderbilt, Phys. Rev. B **47**, 1651 (1993).
 - ² R. Resta, Rev. Mod. Phys. **66**, 899 (1994).
 - ³ D. Vanderbilt and R. D. King-Smith, Phys. Rev. B **48**, 4442 (1993).
 - ⁴ W. Kohn and L. J. Sham, Phys. Rev. **140**, A1133 (1965).
 - ⁵ R. W. Nunes and D. Vanderbilt, Phys. Rev. Lett. **73**, 712 (1994).
 - ⁶ I. Souza, J. Íñiguez, and D. Vanderbilt, Phys. Rev. Lett. **89**, 117602 (2002).
 - ⁷ P. Umari and A. Pasquarello, Phys. Rev. Lett. **89**, 157602 (2002).
 - ⁸ P. Lenarczyk and M. Luisier, eprint arXiv:cond-mat/1910.09015 (2019).
 - ⁹ P. Chandra and P. B. Littlewood, “A Landau primer for ferroelectrics,” in *Physics of Ferroelectrics: A Modern Perspective* (Springer Berlin Heidelberg, Berlin, Heidelberg, 2007) pp. 69–116.
 - ¹⁰ P. Lenarczyk and M. Luisier, in *2016 International Conference on Simulation of Semiconductor Processes and Devices (SISPAD)* (2016) pp. 311–314.
 - ¹¹ N. Sai, K. M. Rabe, and D. Vanderbilt, Phys. Rev. B **66**, 104108 (2002).
 - ¹² O. Diéguez and D. Vanderbilt, Phys. Rev. Lett. **96**, 056401 (2006).
 - ¹³ R. W. Nunes and X. Gonze, Phys. Rev. B **63**, 155107 (2001).
 - ¹⁴ R. E. Cohen and H. Krakauer, Ferroelectrics **136**, 65 (1992).
 - ¹⁵ R. D. King-Smith and D. Vanderbilt, Ferroelectrics **136**, 85 (1992).
 - ¹⁶ N. Marzari, A. A. Mostofi, J. R. Yates, I. Souza, and D. Vanderbilt, Rev. Mod. Phys. **84**, 1419 (2012).
 - ¹⁷ O. Zienkiewicz, R. Taylor, and J. Zhu, in *The Finite Element Method Set (Sixth Edition)*, edited by O. Zienkiewicz, R. Taylor, and J. Zhu (Butterworth-Heinemann, Oxford, 2005) sixth edition ed., pp. 54 – 102.
 - ¹⁸ H. Hellmann, *Einführung in die Quantenchemie* (Deuticke, Leipzig, 1937).
 - ¹⁹ R. P. Feynman, Phys. Rev. **56**, 340 (1939).
 - ²⁰ N. A. Spaldin, Journal of Solid State Chemistry **195**, 2 (2012).
 - ²¹ R. McWeeny, Rev. Mod. Phys. **32**, 335 (1960).
 - ²² E. B. Stechel, A. R. Williams, and P. J. Feibelman, Phys. Rev. B **49**, 10088 (1994).
 - ²³ R. Resta, Phys. Rev. Lett. **80**, 1800 (1998).
 - ²⁴ P. Pulay, Mol. Phys. **17**, 197 (1969).
 - ²⁵ M. C. Payne, M. P. Teter, D. C. Allan, T. A. Arias, and J. D. Joannopoulos, Rev. Mod. Phys. **64**, 1045 (1992).
 - ²⁶ L. Kleinman and D. M. Bylander, Phys. Rev. Lett. **48**, 1425 (1982).
 - ²⁷ M. M. G. Alemany, M. Jain, L. Kronik, and J. R. CheLIKowsky, Phys. Rev. B **69**, 075101 (2004).
 - ²⁸ K. Hirose, *First-principles calculations in real-space formalism : electronic configurations and transport properties of nanostructures* (Imperial College Press, London, 2005).
 - ²⁹ X. Andrade, D. Strubbe, U. De Giovannini, A. H. Larsen, M. J. T. Oliveira, J. Alberdi-Rodriguez, A. Varas, I. Theophilou, N. Helbig, M. J. Verstraete, L. Stella, F. Nogueira, A. Aspuru-Guzik, A. Castro, M. A. L. Marques, and A. Rubio, Phys. Chem. Chem. Phys. **17**, 31371 (2015).
 - ³⁰ E. L. Briggs, D. J. Sullivan, and J. Bernholc, Phys. Rev. B **54**, 14362 (1996).
 - ³¹ D. Vanderbilt and R. D. King-Smith, eprint arXiv:cond-

- mat/9801177 (1998).
- 32 D. Vanderbilt and S. G. Louie, Phys. Rev. B **30**, 6118 (1984).
 - 33 W. H. Press, S. A. Teukolsky, W. T. Vetterling, and B. P. Flannery, *Numerical Recipes 3rd Edition: The Art of Scientific Computing*, 3rd ed. (Cambridge University Press, New York, NY, USA, 2007).
 - 34 X. Gonze and C. Lee, Phys. Rev. B **55**, 10355 (1997).
 - 35 X. Gonze, Phys. Rev. B **55**, 10337 (1997).
 - 36 A. Togo and I. Tanaka, Scripta Materialia **108**, 1 (2015).
 - 37 N. Marzari and D. Vanderbilt, First-Principles Calculations for Ferroelectrics Aip Conference Proceedings, 146 (1998).
 - 38 D. D. Johnson, Phys. Rev. B **38**, 12807 (1988).
 - 39 L. Mones, G. Csanyi, and C. Ortner, Scientific Reports **8**, 13991 (2018).
 - 40 M. V. Fernández-Serra, E. Artacho, and J. M. Soler, Phys. Rev. B **67**, 100101 (2003).
 - 41 H. Bilz, G. Benedek, and A. Bussmann-Holder, Phys. Rev. B **35**, 4840 (1987).
 - 42 J. R. Chelikowsky, “Parsec quantum mechanics applied to materials,” <http://parsec.ices.utexas.edu/>, accessed: 2019-08-01.
 - 43 G. Shirane, H. Danner, and R. Pepinsky, Phys. Rev. **105**, 856 (1957).
 - 44 G. Shirane, R. Pepinsky, and B. C. Frazer, Acta Crystallographica **9**, 131 (1956).
 - 45 D. Vanderbilt, Journal of Physics and Chemistry of Solids **61**, 147 (2000).
 - 46 J. R. Chelikowsky, Journal of Physics D: Applied Physics **33**, R33 (2000).
 - 47 J. L. Martins, “Atomic code,” <http://bohr.inesc-mn.pt/~jlm/pseudo.html>, accessed: 2019-08-01.
 - 48 N. Troullier and J. L. Martins, Phys. Rev. B **43**, 1993 (1991).
 - 49 S. G. Louie, S. Froyen, and M. L. Cohen, Phys. Rev. B **26**, 1738 (1982).
 - 50 L. Kronik, I. Vasiliev, M. Jain, and J. R. Chelikowsky, The Journal of Chemical Physics **115**, 4322 (2001).
 - 51 J. R. Chelikowsky, N. Troullier, and Y. Saad, Phys. Rev. Lett. **72**, 1240 (1994).
 - 52 X. Gonze, P. Ghosez, and R. W. Godby, Phys. Rev. Lett. **74**, 4035 (1995).
 - 53 R. M. Martin and G. Ortiz, Phys. Rev. B **56**, 1124 (1997).
 - 54 P. Ghosez, X. Gonze, and R. W. Godby, Phys. Rev. B **56**, 12811 (1997).
 - 55 D. M. Ceperley and B. J. Alder, Phys. Rev. Lett. **45**, 566 (1980).
 - 56 J. P. Perdew and A. Zunger, Phys. Rev. B **23**, 5048 (1981).
 - 57 J. Kim, F. Mauri, and G. Galli, Phys. Rev. B **52**, 1640 (1995).
 - 58 H. J. Monkhorst and J. D. Pack, Phys. Rev. B **13**, 5188 (1976).
 - 59 W. J. Merz, Phys. Rev. **91**, 513 (1953).
 - 60 S. Salahuddin and S. Datta, Nano Letters **8**, 405 (2008).
 - 61 K. M. Rabe and P. Ghosez, “First-principles studies of ferroelectric oxides,” in *Physics of Ferroelectrics: A Modern Perspective* (Springer Berlin Heidelberg, Berlin, Heidelberg, 2007) pp. 117–174.
 - 62 V. V. Nemoshkaleiko and A. N. Timoshevskii, physica status solidi (b) **127**, 163 (1985).
 - 63 L. T. Hudson, R. L. Kurtz, S. W. Robey, D. Temple, and R. L. Stockbauer, Phys. Rev. B **47**, 1174 (1993).
 - 64 L. F. Mattheiss, Phys. Rev. B **6**, 4718 (1972).
 - 65 P. Pertosa and F. M. Michel-Calendini, Phys. Rev. B **17**, 2011 (1978).
 - 66 P. Pertosa, G. Hollinger, and F. M. Michel-Calendini, Phys. Rev. B **18**, 5177 (1978).
 - 67 V. G. Gavrilachenko, R. I. Spinko, M. A. Martynenko, and E. G. Fesenko, Sov. Phys. Solid State **12**, 1203 (1970).
 - 68 S. F. Yuk, K. Pitike, S. M. Nakhmanson, M. Eisenbach, Y. W. Li, and V. Cooper, Scientific Reports **7**, 43482 (2017).